Intermetallics 172 (2024) 108380

Contents lists available at ScienceDirect

Intermetallics

journal homepage: www.elsevier.com/locate/intermet

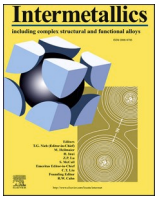

Influence of the Nb–Al ratio on homogenization behavior and hierarchical microstructures in high-entropy superalloys

Yiqin Ma [a], Qiuying Ji [b,c], Sieglind Ngai [b,c], Jingzhen Li [f], Michael J. Pavel [g], Mark L. Weaver [g], Peng Zhang [a], Wei Li [a,**], Yuan Wu [h], Florian Vogel [d,e,*]

[a] Institute of Advanced Wear & Corrosion Resistant and Functional Materials, Jinan University, Guangzhou, 510632, Guangdong Province, China
[b] Guangdong Provincial Key Laboratory for Processing and Forming of Advanced Metallic Materials, Guangzhou, 510640, Guangdong Province, China
[c] School of Mechanical and Automobile Engineering, South China University of Technology, Guangzhou, 510640, Guangdong Province, China
[d] Pico Electron Microscopy Center, Innovation Institute for Ocean Materials Characterization Technology, Center for Advanced Studies in Precision Instruments, Hainan University, Haikou, 570228, Hainan Province, China
[e] Key Laboratory of Pico Electron Microscopy of Hainan Province, Hainan University, Haikou, 570228, Hainan Province, China
[f] Institute of Mass Spectrometry and Atmospheric Environment, Jinan University, Guangzhou, 510632, Guangdong Province, China
[g] Department of Metallurgical and Materials Engineering, The University of Alabama, Tuscaloosa, AL, 35401-0202, USA
[h] State Key Laboratory for Advanced Metals and Materials Beijing, University of Science and Technology Beijing, 100083, Beijing, China

ARTICLE INFO

Keywords:
High-entropy superalloy
Alloy design
Segregation
Hierarchical microstructure
Mechanical properties

ABSTRACT

In this investigation, we explore the impact of the Nb–Al ratio on the microstructural and mechanical properties of high-entropy superalloys (HESAs), focusing on hierarchical microstructures. Utilizing a series of HESAs with varying Nb–Al ratios, our study employs advanced characterization techniques, including differential scanning calorimetry (DSC) for thermal analysis, electron probe micro-analyzer (EPMA) for compositional analysis for the design of a homogenization treatment at 1500 K/24 h. Transmission electron microscopy (TEM) reveals that the increasing Nb–Al ratio refines the γ' precipitates and influences the size and volume fraction of embedded hierarchical γ particles. ThermoCalc equilibrium phase analysis and Vegard's-law calculations reveal a minimal lattice misfit between these phases, highlighting the interplay between Nb–Al ratio and phase stability. The increasing Nb–Al ratio inhibits the formation of hierarchical γ particles. We observe an enhancement in hardness from 433 HV to 492 HV with an increasing Nb–Al ratio. This study provides valuable insights into the role of Nb and the Nb–Al ratio in HESAs with hierarchical microstructures, demonstrating its significant influence on γ particle formation within γ' precipitates and mechanical strength. The findings advance our understanding of alloy design and pave the way for developing advanced HESAs for high-temperature applications.

1. Introduction

The advent of high entropy superalloys (HESAs) represents a significant shift in the landscape of alloy design, moving away from traditional alloy frameworks to explore the rich and complex compositional space of multi-principal elements [1–3]. Characterized by their exceptional mechanical properties, HESAs are born from the high-entropy alloy (HEA) concept, which employs a balanced mix of multiple principal elements to achieve remarkable material characteristics [1,2]. For instance, HEAs such as the CoCrFeMnNi have displayed extraordinary tensile strength and ductility at cryogenic temperatures, while others like $Al_{0.5}CoCrFe_{0.5}NiTi_{0.5}$ have shown impressive compressive strength at room temperature due to the presence of intermetallic phases like σ, B2, and Laves [1,4].

A key challenge in the field of HEAs, and by extension HESAs, is the maintenance of high tensile strength at elevated temperatures. This issue is particularly critical in applications such as power plants and aircraft engines, where materials are subjected to harsh, high-temperature environments. Traditional superalloys, typically Ni-based, achieve high-temperature strength through the formation of coherent $Ni_3(Al,Ti)$ $L1_2$ structured γ' precipitates in an A1 solid solution γ matrix. This concept of precipitation strengthening has been increasingly applied to HESAs, leading to the development of alloys with superior high-temperature strength [2,5–7].

* Corresponding author. Key Laboratory of Pico Electron Microscopy of Hainan Province, Hainan University, Haikou, 570228, Hainan Province, China.
** Corresponding author.
E-mail addresses: liweijnu@126.com (W. Li), fvogel@hainanu.edu.cn (F. Vogel).

https://doi.org/10.1016/j.intermet.2024.108380
Received 21 February 2024; Received in revised form 20 May 2024; Accepted 13 June 2024
Available online 26 June 2024

However, the elevated temperature tensile strength of HESAs can be limited by the fractions and solvus temperatures of the strengthening phases [8–13]. To enhance these properties, alloy designs that increase the fraction and solvus temperature of phases like $L1_2$ are needed. The concept of HESA extends the high entropy idea by including a higher content of Ni, which facilitates the formation of thermally stable $L1_2$ γ' precipitates while maintaining significant configurational entropy [2].

In parallel with the development of HESAs, the concept of hierarchical microstructures has emerged as an innovative strategy to further enhance mechanical properties, especially creep resistance [2,14,15]. Hierarchical microstructures are characterized by the presence of additional particles, often γ phase, within the host precipitates [16–20]. This structural complexity has been shown to improve creep resistance and overall mechanical performance in both Fe-based and Ni-based alloys, as well as in Co-based and high-entropy alloys [5,21,22].

A critical challenge in leveraging hierarchical microstructure strengthening lies in addressing the metastability of these structures at elevated temperatures [2,16,23]. At such conditions, hierarchical particles exhibit two major behaviors: They either continue growth, leading to the splitting of the precipitate host phase [14,24–26], or dissolve within the host phase over time [27–29]. Both metastability pathways ultimately contribute to a reduction in thermo-mechanical strength. Therefore, a pivotal issue that requires resolution is: How can we effectively control and customize morphology, size, and volume fraction of hierarchical particles to attain both temporal and thermal stability?

Our choice of the alloy system, inspired by *Chen* et al., was strategically guided by its potential to form hierarchical microstructures known to enhance mechanical properties [2]. These structures, which introduce secondary γ phase particles within primary γ' precipitates, not only improve creep resistance but also extend the high-temperature capabilities of the alloys. This unique combination of features makes the alloy an ideal candidate for advanced engineering applications that require superior mechanical performance and stability.

Our current study on HESAs explores the integration of these two innovative concepts: The high entropy approach and the exploitation of hierarchical microstructures. We focus on a specific HESA, which incorporates Nb as a γ'-forming element, to study its impact on the alloys' homogenization behavior and formation of hierarchical γ particles. Through our research, we aim to induce hierarchical microstructures with enhanced temporal stability. By exploring the phase transformation pathways and understanding the metastability of these structures, we strive to provide a new pathway for the development of advanced high-temperature materials. This work not only contributes to the advancement of high entropy materials but also opens new possibilities for the application of hierarchical microstructures in the space of high-temperature alloy design. This research thus represents a significant step forward in the development of novel high entropy superalloys, providing valuable insights for the design of future advanced materials.

2. Materials and methods

2.1. Sample preparation

Polycrystalline alloys were fabricated with the compositions listed in Table 1, where the Nb content was increased by 0.2 at.% steps, balanced by reducing the Al content. These alloys were prepared by the arc-melting method. The process utilized a water-cooled copper base plate and a tungsten electrode. High-purity materials, including Ni, Al, and Ti (with purities of 5 N, 5 N, and 4 N, respectively), were used for ingot production, while the purity of the remaining elements ranged from 3 N to 4 N. For simplicity, the alloy variants will hereafter be referred to as Nb1.2, Nb1.4, Nb1.6 and Nb1.8.

Table 1
Nominal composition of experimental high-entropy superalloys (in at.%).

Alloy name	Ni	Co	Al	Fe	Cr	Ti	Nb	Mo	W
Nb1.2 (base)	48.3	16.9	10.2	8.9	7.4	5.8	1.2	0.9	0.4
Nb1.4	48.3	16.9	10.0	8.9	7.4	5.8	1.4	0.9	0.4
Nb1.6	48.3	16.9	9.8	8.9	7.4	5.8	1.6	0.9	0.4
Nb1.8	48.3	16.9	9.6	8.9	7.4	5.8	1.8	0.9	0.4

2.2. Heat treatment

The as-cast ingots were sliced approximately parallel to the growth direction of dendrites, following a <001> orientation, resulting in slices with a thickness of 2 mm. These slices were subjected to a homogenization process within a vacuum tube furnace under a continuous flow of argon (80 ml min^{-1}). The temperature and duration of the homogenization treatment for each alloy were determined based on differential scanning calorimetry (DSC) measurements and diffusion calculations, considering dendrite spacing. All alloys were homogenized simultaneously at a ramp process from room temperature to 1500 K for within 20 h followed by holding 1500 K for 4 h, for simplicity referred to as 1500 K/24 h. Hereafter all samples were taken out and air cooled.

2.3. Characterization

The specimens designated for light microscopy (LM), scanning electron microscopy (SEM), and electron probe microanalyzer (EPMA) analysis by wavelength dispersive spectrometry (WDS) underwent a sequence of mechanical grinding and three successive polishing steps. Polishing and subsequent etching of the samples is detailed elsewhere [30].

Reaction temperatures were determined using DSC and ThermoCalc simulations (TCS).

EPMA analysis was performed using a *Jeol JXA-8100* Electron Microprobe, operating at 15 kV. Elemental mappings covered a 500 × 500 μm^2 area for both as-cast and homogenized samples. Point measurements were taken in the dendrite core (DC) and inter-dendritic (ID) regions, with 10 points in each region of as-cast samples and a 3 × 3 point grid array in homogenized samples. The spacing between points was approximately 30–50 μm. Analysis conditions included a 20 nA current, 20 kV voltage, and 1–2 μm spot size. Standard measurements were conducted prior to analysis.

TEM samples were prepared using a *ThermoFisher Helios 5 CX* focused ion beam (FIB) instrument. Prior to the FIB lift-out procedures, the microstructure's orientation was considered to ensure a <001> orientation for the TEM sample. Thinning was achieved initially with 30 kV Ga^+ ions, followed by a final low-kV step at 2 kV to eliminate surface damage.

TEM imaging was carried out using a *ThermoFisher Talos F200i*, operating at 200 kV. Dark-field imaging was achieved through the utilization of an $L1_2$ superlattice reflection.

DSC analysis was executed on all as-cast samples employing a *Mettler TGA/DSC 3+* apparatus under a flowing argon environment at 50 ml min^{-1}, with a heating rate of 10 K min^{-1}. The mass of each DSC sample was about (28 ± 2) mg.

For the determination of reaction temperatures, ThermoCalc based on the CALPHAD method [31] and the TCNi12 Nickel-based superalloys database [32] were employed.

The Vickers hardness was measured with a load of 9.8 N and a dwell time of 10 s on a *T-VICTORY 1000 Pro* Vickers Hardness tester. Each hardness value is the average of at least 10 indentations.

2.4. Microstructure analysis

To determine the volume fraction of DC and ID regions from compositions, the lever-rule approach derived from the mass balance equation for each element was implemented, as described elsewhere [33].

The area fraction F_p of γ' precipitates are considered to derive the

volume fraction V_p of γ' precipitates from SEM image analysis, as detailed elsewhere [34].

The phase composition-based volume fractions from ThermoCalc data at 1023 K was obtained via the lever-rule approach (mass balance equation).

3. Results & discussion

3.1. Design of homogenization treatment

3.1.1. As-cast microstructure

Fig. 1 is a series of light microscopy (LM) images depicting typical dendritic as-cast microstructures of four high entropy superalloys (HESA) with varying Nb–Al ratio (compositions see Table 1). For simplicity, these alloys will be referred to as Nb1.2, Nb1.4, Nb1.6 and Nb1.8 (Fig. 1a–d, respectively). In all alloys, the dendrite core (DC) regions appear bright, while the interdendritic (ID) regions appear dark, marked by yellow and blue arrows, respectively (Fig. 1a). The image contrast originates from the preferential etching of ID regions, causing protruding DCs and valleys where ID regions are, affecting the reflection of light. The arc-melted polycrystalline samples were cut parallel to the growth direction of dendrites (close to <001> directions), approximated by considering the solidification direction of the button ingot.

The dendritic as-cast microstructure is schematically shown in Fig. 1e, where the x-y view indicates the PDAS, λ in a <001> growth direction of the dendrite cores, from which the experimental diffusion distance x_i^{exp}, between DC and ID regions is derived (**Eq. (1)**). The x-z view highlights the side view of dendrite cores like images shown in Fig. 1a–d. To determine the time needed for homogenization it is necessary to know the diffusion distance x, that the alloying elements need to overcome between DC and ID regions. Fig. 1e highlights how the diffusion distance x_i^{exp}, was derived from measuring the primary dendrite arm spacing (PDAS) λ, which is the distance between dendrite cores (measured from light microscopy images as shown in Fig. 1):

$$x_i^{exp} = \lambda^{-0.5} \quad \text{Eq. 1}$$

The measured and calculated values for λ and x_i^{exp} are summarized in Table 2.

Table 2 lists the average values for the PDAS, λ_{avg} and the derived diffusion distances x_i^{exp} between DC and ID regions for our four experimental HESA. The average λ_{avg} values are between 66 and 73 μm, with no significant impact of the increasing Nb–Al ratio (within the error). We attribute the relatively large error (standard deviation), to small deviations from an ideal <001> direction when cutting the ingots. In contrast to single crystal cast superalloys, where the cooling rate is slower (0.2–3.9 K s^{-1}) [35], and λ_{avg} values are within 250–400 μm, our alloys were prepared by arc-melting, where rapid cooling occurs upon solidification, resulting in smaller λ_{avg} values [36,37].

Table 2
Average values for $PDAS_{avg}$ and the derived diffusion distances x_i^{exp} between DC and ID regions for the HESAs Nb1.2, Nb1.4, Nb1.6 and Nb1.8 alloys in as-cast condition.

Alloy	λ (μm)	x_i^{exp} (μm)
Nb1.2	70 ± 36	50 ± 27
Nb1.4	66 ± 34	47 ± 24
Nb1.6	70 ± 38	49 ± 26
Nb1.8	73 ± 45	51 ± 30
Average, $\bar{x}_i^{exp}$	70 ± 38	50 ± 27

3.1.2. Homogenization temperature and time

Fig. 2 highlights how temperature window and time for homogenization are determined from comparing DSC to ThermoCalc data and diffusion calculations. Fig. 2a shows DSC heating profiles of the as-cast Nb1.2, Nb1.4, Nb1.6 and Nb1.8 alloys (black, blue, red, and green, respectively), obtained at a heating rate of 10 K min^{-1}. The reaction temperatures obtained from DSC are given in Table 3. ThermoCalc equilibrium phase volume fractions of the γ matrix (green), γ' precipitate (orange), liquid (purple) and other minor (grey) phases are shown in Fig. 2b, where brighter shades of one color represent the increasing Nb–Al ratio. A further enlarged view of the region between 1400 and 1600 K marked by a blue box is shown in Fig. 2c, highlighting the γ' precipitate solvus (T_ γ'_{sol}), and the alloys' solidus (T_a_{sol}) and liquidus (T_a_{liq}) temperatures, all decreasing with increasing Nb–Al ratio (also given in Table 3). In Fig. 2d reaction temperatures from DSC (open symbols) data are compared to those from ThermoCalc simulations (solid symbols), where the γ' precipitate solvus (orange circle), and the alloys' solidus (green triangle) and liquidus (purple square) temperatures are indicated. Dissolution of γ' generally occurs between 1450 and 1490 K (DSC), whereby ThermoCalc predicted values are around 1430 K. The consistent trend between DSC and ThermoCalc data is the decrease of the γ' solvus temperature with increasing Nb–Al ratio. The

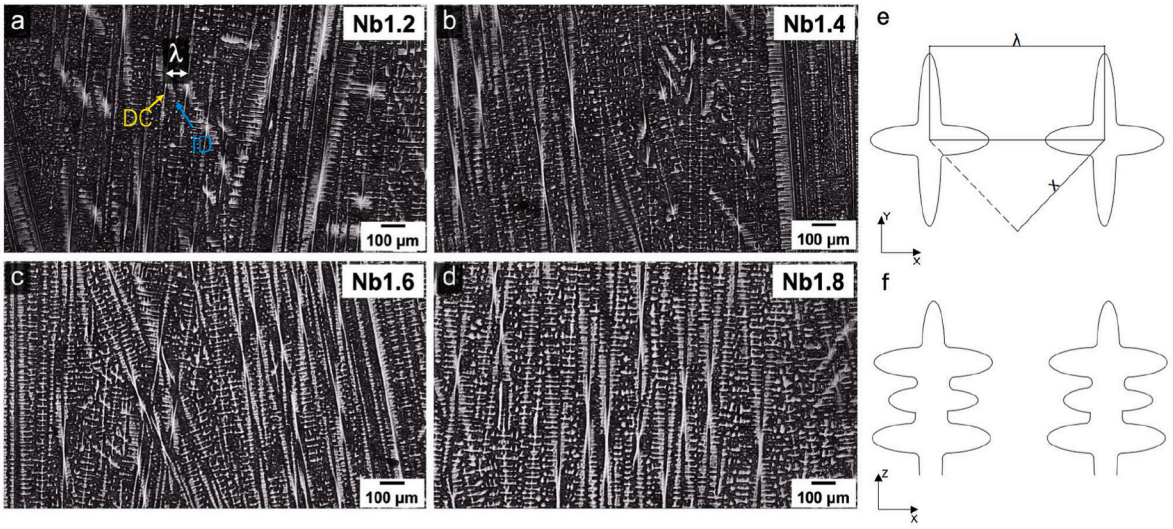

Fig. 1. Light microscopy images of the dendritic as-cast microstructure of high-entropy superalloys with varying Nb–Al ratio. Shown in (**a-d**): Nb1.2, Nb1.4, Nb1.6 and Nb1.8, respectively. Schematic view of dendrites in (**e**) growth direction illustrating primary dendrite arm spacing (PDAS) λ and the DC-ID distance x. (**f**) Schematic side view of dendrites. Compositions listed in Table 1.

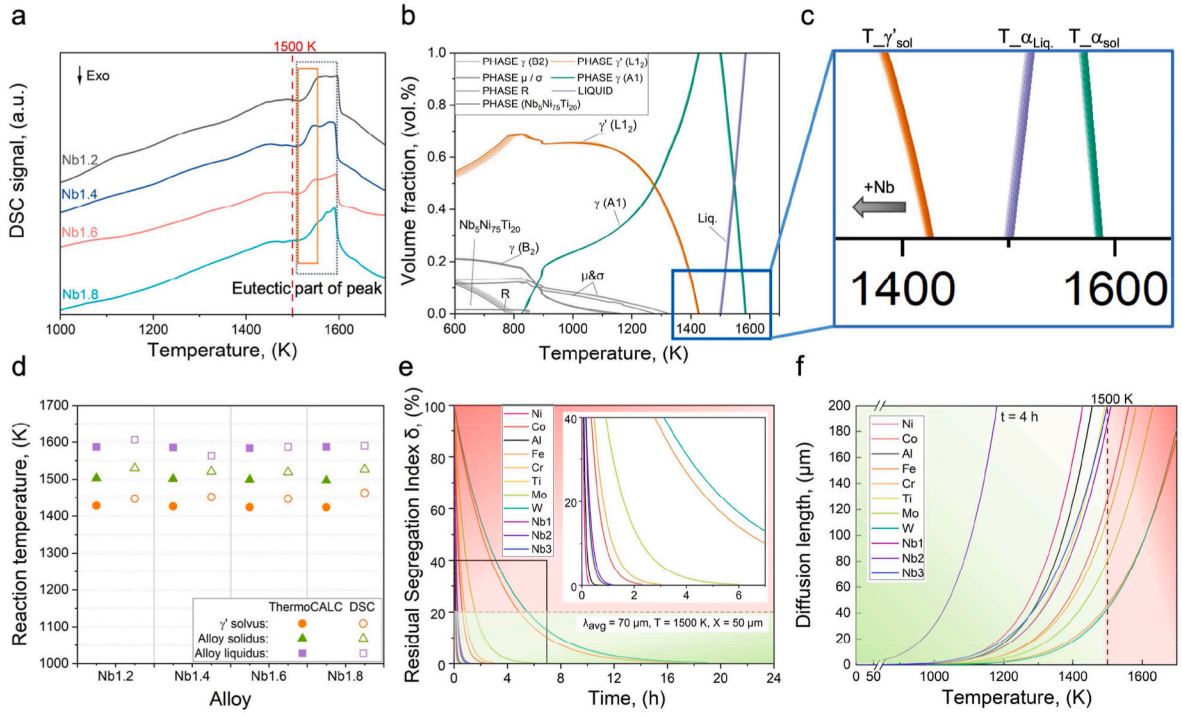

Fig. 2. Thermodynamic and diffusion parameters of experimental HESAs Nb1.2, Nb1.4, Nb1.6 and Nb1.8: (**a**) DSC heating profiles (10 K min^{-1}) of samples in as-cast condition. (**b**) ThermoCalc equilibrium phase volume fractions of the γ matrix and the γ' precipitate phases. (**c**) Enlarged view of the temperature range between 1400 and 1600 K (**d**) Comparison of reaction temperatures, γ' solvus (squares), alloy solidus (triangles) and liquidus (circles) between DSC and ThermoCalc simulations. (**f**) Theoretical residual segregation index $\delta_i^{th}(t)$ of each element i at a temperature of 1500 K, calculated based on **Eq. (2)** using the average diffusion distance $\bar{x}_i^{exp}$ (derived from λ) of all alloys (Table 2). (**e**) Possible diffusion distance x of each element i and diffusion parameters (Table 4).

Table 3
Comparison of reaction temperatures from DSC and ThermoCalc data of HESAs Nb1.2, Nb1.4, Nb1.6 and Nb1.8: γ' solvus, the alloys' solidus and liquidus temperatures are given (as-cast condition).

	Nb1.2		Nb1.4		Nb1.6		Nb1.8	
	ThermoCalc	DSC	ThermoCalc	DSC	ThermoCalc	DSC	ThermoCalc	DSC
γ' Solvus (K)	1428.5	1447.7	1426.7	1451.8	1424.1	1447.0	1423.6	1463.2
Solidus (K)	1503.0	1530.3	1501.0	1521.2	1498.9	1519.2	1496.8	1526.7
Liquidus (K)	1587.3	1606.5	1585.7	1563.2	1584.0	1587.2	1582.4	1590.5

alloys' solidus temperatures around 1500 K are in excellent agreement between DSC and ThermoCalc (within ±10 K). The alloys' liquidus temperatures are within 1600 K and decrease slightly with increasing Nb–Al ratio. Good agreement is observed between DSC and ThermoCalc data. In our experimental alloys, the Nb content increases in 0.2 at.% increments (balanced with Al) compared to the base alloy (Nb1.2), and the concentration of the remainder of alloying elements (Ni, Co, Fe, Cr, Ti, Mo and W) is constant (Table 1). In a similar Ni-based superalloy (without Co), the γ' solvus temperature was also found to decrease with increasing Nb and Al contents (balanced with Ni) [38]. In contrast, a 5 K increase of the γ' solvus temperature was observed for a 1 at.% Nb containing alloy vs. the 0 at.% Nb counterpart [39].

From DSC and ThermoCalc data in Fig. 2d, we derive a temperature window for homogenization between 1450 and 1510 K. Here, the higher the temperature, the shorter the time needed. Lastly, our DSC data confirm the homogenization temperature of 1500 K used for the base alloy [2,36,40], to be suitable for our modified alloys with increased Nb–Al ratio.

To determine the homogenization time at 1500 K, we consider two common methods:

(1) the residual segregation index δ_i^{th} as function of time at 1500 K (Fig. 2e) after **Eq. (2)**, and

(2) the theoretically possible diffusion distance x_i^{th} as function of temperature (Fig. 2f) after **Eq. (3)**, for an element i. Both methods utilize diffusion parameters given in Table 4. For Nb, diffusion parameters from three different references were considered [41–43].

The residual segregation index is defined as:

$$ln\ \delta_i^{th} = -\frac{4\pi^2}{x_i^{exp2}} D_{0,i}\, exp\left(-\frac{Q_i}{RT}\right) t \qquad \text{Eq. 2}$$

where x_i^{exp} is the distance between DC and ID regions (indicated in Fig. 1e), Q_i is the activation energy, R is the gas constant, $D_{0,i}$ is the frequency factor for volume diffusion, T is the temperature, and t is the time, respectively. All diffusion parameters are listed in Table 4.

The theoretically possible diffusion distance is defined as:

$$x_i^{th} = \sqrt{D_0 \exp\left(-\frac{Q}{RT}\right) t} \qquad \text{Eq. 3}$$

Generally, when $\delta_i^{th} < 20$ %, a satisfactory level of homogenization is achieved. Fig. 2e reveals $\delta_i^{th} < 20$ % for i = Fe and W when $t < 6$ h, and for i = Ni, Co, Al, Cr, Ti, Mo, Nb when t < 2 h (green shaded area). The

Table 4
Diffusion parameters for diffusion in Ni solid solution. The frequency factor for volume diffusion D_0 and the activation energy for diffusion Q of each element in nickel-based superalloys. All values taken from the literature (see references).

Element		D_0 (m^2 s^{-1})	Q (J mol^{-1})	Material/Phase	Reference
Ni		1.00×10^{-03}	271,960	Ni/Ni–45 A l (at.%) diffusion couple	*Janssen* 1973 [45]
Co		2.97×10^{-04}	281,605	First principles calculations	*Qiong et al.,* 2012 [46]
Al		1.50×10^{-03}	282,000	γ/γ' diffusion couple	Karunaratne et al., 2001 [47]
Fe		0.44×10^{-04}	283,257	Binary Fe–Ni Austenite	*Dean et al.,* 1986 [48]
Cr		1.10×10^{-04}	272,400	Inconel-600 coated with pure Cr	*Dpruthi et al.,* 1977 [49]
Ti		3.70×10^{-04}	272,000	γ/γ' diffusion couple	*Karunaratne et al.,* 2001 [47]
Nb	Nb 1	8.8×10^{-05}	257,000	Ni/Ni–4Nb (at.%) diffusion couples	*Karunaratne et al.,* 2005 [41]
	Nb 2	1.04×10^{-04}	202,590	Ni/Ni-7.1Nb (at.%) diffusion couples	*Heijwegen et al.,* 1973 [42]
	Nb 3	1.618×10^{-05}	234,100	Ni/Ni–4Nb (at.%) diffusion couples	*Sohrabi et al.,* 2020 [43]
Mo		1.15×10^{-04}	281,300	Ni/Ni-6.5Mo (at.%) diffusion couples	*Karunaratne et al.,* 2005 [41]
W		2.07×10^{-04}	304,040	Ni/Ni–4W (at.%) diffusion couple	*Walsh et al.,* 1969 [50]

area marked by a black box is further magnified and shown as inset.

Fig. 2f demonstrates the theoretical possible diffusion distance x_i^{th} for element i (with i = Ni, Co, Al, Fe, Cr, Ti, Mo, W or Nb) in our HESAs as function of temperature up to the melting point (~1700 K). x_i^{th} is calculated using diffusion parameters from the literature (summarized in Table 4) and the time t is set as t = 4 h. For Nb, diffusion parameters from three different references were considered [41–43]. The average diffusion distance between DC and ID regions of all 4 alloys, $\overline{x}_i^{exp}$ as the threshold distance of approximately 50 μm, is indicated by a horizontal dashed line. Sufficient mobility, to equalize concentration differences between DC and ID regions is indicated when the condition $x_i^{th} > \overline{x}_i^{exp}$ is met (Fig. 2f). A theoretically possible diffusion distance of $x_i^{th} > 50$ μm is reached for all alloying elements at 1500 K within 4 h (indicated by the green shaded area in Fig. 2f). Here, also Fe and W seem to diffuse much slower compared to the other alloying elements. Considering satisfaction of the $\delta_i^{th} < 20$ % criterion gives a 50 % longer time compared to the $x_i^{th} > 50$ μm criterion. We rationalize that the applied homogenization treatment includes a ramp from room temperature up to 1500 K within 20 h (at a nearly linear temperature increase of 1.25 K min^{-1}) followed by holding 1500 K for 4 h. In Ni-based superalloys, considerable diffusion begins above about 1200 K, which is reached after 15 h into the ramp process. This leaves another 5 h within 1200–1500 K where x_i^{th} reaches from about 5 to 50 μm, depending on the element, then followed by holding 1500 K for 4 h. We hence conclude that the homogenization parameters of T = 1500 K and t = 4 h, are theoretically sufficient to homogenize our alloys [44].

3.2. Characterization of segregation and homogenization

Fig. 3 presents an example of electron probe micro-analyzer (EPMA) elemental maps for all alloying elements in a Nb1.6 alloy in the as-cast (Fig. 3a) and homogenized (Fig. 3b) conditions. We note that comparable results were obtained for the other alloys, and hence they are omitted here. The elemental maps (Fig. 3a) reveal a clear partitioning trend, i.e., γ (matrix) phase-forming elements (Ni, Co, Fe, Cr and W) segregate towards DC regions, whereas γ' (precipitate) phase-forming elements (Al, Ti and Nb) segregate towards ID regions. Mild segregation behavior is observed for Ni, Co, Al and Mo. Stronger segregation behavior is revealed by Fe, Cr, Ti, Nb and W. A compositionally uniform distribution of alloying elements is achieved after homogenization (Fig. 3b).

Concentrations from DC and ID regions of as-cast samples are obtained via EPMA point measurements, with the results given in Table 5. Concentrations from point measurements of homogenized samples are given in Table 6. The element concentrations within each region represent averages from 10 points measurements with the associated error as standard deviation.

3.2.1. Partitioning coefficient k'_i

The partitioning behavior of an element i between DC and ID regions is further quantified using the partitioning coefficient k'_i, an indicator that describes the extent of element distribution between the two regions:

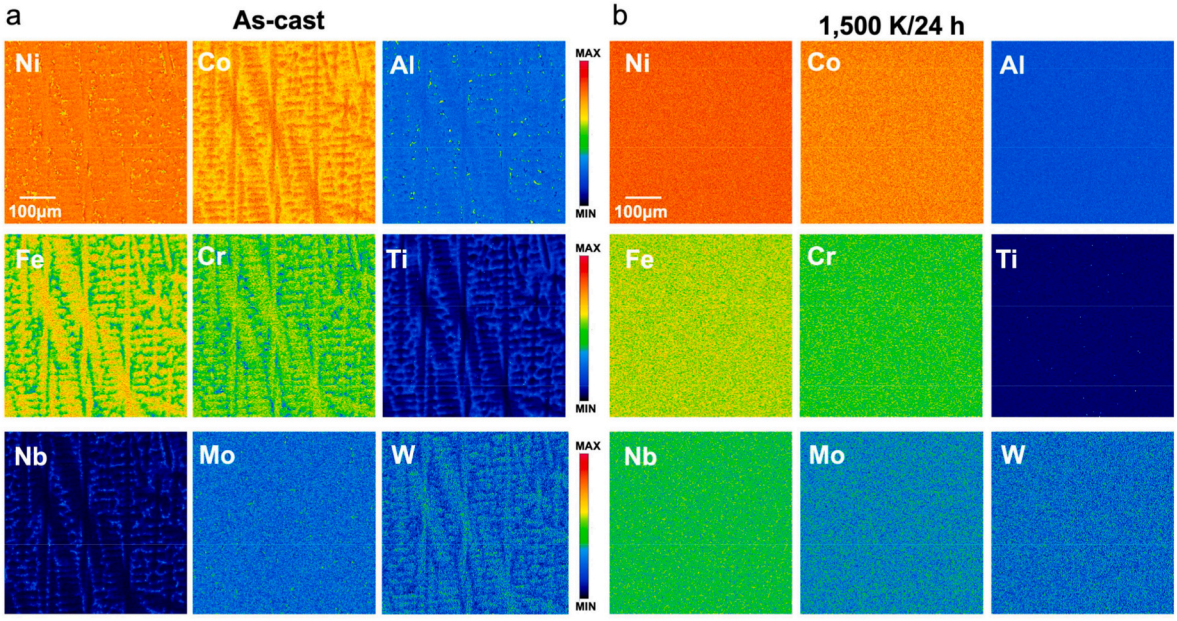

Fig. 3. EPMA elemental maps of a Nb1.6 alloy (exemplary) in (**a**) as-cast and (**b**) homogenized condition (1500 K/24 h). Color scale refers to at.%.

Table 5
EPMA composition data of HESAs Nb1.2, Nb1.4, Nb1.6 and Nb1.8 in as-cast condition. Values from dendrite cores (DC) and interdendritic (ID) regions (each average from ten point measurements) are given in at.%. The errors are standard deviation and calculated based on standard error propagation methods [51].

Alloy	Region	Concentration, (at.%)								
		Ni	Co	Al	Fe	Cr	Ti	Nb	Mo	W
Nb1.2	**ID**	46.80 ± 2.75	16.64 ± 0.86	9.19 ± 1.13	8.19 ± 1.20	7.39 ± 1.67	8.35 ± 0.90	2.22 ± 0.47	0.98 ± 0.31	0.23 ± 0.04
	DC	47.85 ± 0.25	17.64 ± 0.37	10.11 ± 0.27	9.72 ± 0.45	7.90 ± 0.30	4.83 ± 0.62	0.72 ± 0.13	0.87 ± 0.06	0.37 ± 0.05
Nb1.4	**ID**	45.92 ± 2.85	16.54 ± 0.91	10.61 ± 3.20	8.03 ± 1.42	7.07 ± 1.62	8.09 ± 1.74	2.63 ± 1.07	0.92 ± 0.26	0.19 ± 0.07
	DC	47.95 ± 0.52	17.62 ± 0.57	10.05 ± 0.30	9.56 ± 0.72	7.71 ± 0.62	5.00 ± 1.04	0.95 ± 0.31	0.85 ± 0.05	0.32 ± 0.07
Nb1.6	**ID**	47.42 ± 1.74	16.66 ± 0.54	9.40 ± 0.72	8.39 ± 0.95	7.17 ± 1.22	7.61 ± 0.88	2.24 ± 0.44	0.88 ± 0.19	0.24 ± 0.04
	DC	48.08 ± 0.47	17.90 ± 0.74	9.46 ± 0.35	9.74 ± 0.86	7.87 ± 0.59	4.71 ± 1.29	1.03 ± 0.48	0.82 ± 0.05	0.39 ± 0.10
Nb1.8	**ID**	45.48 ± 3.38	17.21 ± 0.76	8.79 ± 1.59	8.67 ± 1.11	7.62 ± 1.33	7.55 ± 1.82	3.37 ± 2.51	1.06 ± 0.36	0.24 ± 0.09
	DC	47.98 ± 0.26	17.67 ± 0.46	9.86 ± 0.29	9.75 ± 0.51	7.82 ± 0.32	4.80 ± 0.65	0.98 ± 0.21	0.77 ± 0.02	0.37 ± 0.06

Table 6
EPMA composition data of HESAs Nb1.2, Nb1.4, Nb1.6 and Nb1.8 in the homogenized condition (1500 K/24 h). Average values from ten individual point measurements are given in at.%. The errors are standard deviation and calculated based on standard error propagation methods [51].

Alloy	Concentration, (at.%)								
	Ni	Co	Al	Fe	Cr	Ti	Nb	Mo	W
Nb1.2	48.08 ± 0.25	17.21 ± 0.15	10.17 ± 0.13	8.99 ± 0.18	7.35 ± 0.19	5.90 ± 0.08	1.11 ± 0.03	0.84 ± 0.05	0.35 ± 0.02
Nb1.4	47.69 ± 0.38	17.18 ± 0.18	10.07 ± 0.16	9.11 ± 0.20	7.48 ± 0.31	5.99 ± 0.11	1.32 ± 0.03	0.88 ± 0.05	0.30 ± 0.02
Nb1.6	48.14 ± 0.25	17.25 ± 0.14	9.48 ± 0.21	9.21 ± 0.17	7.50 ± 0.20	5.79 ± 0.11	1.45 ± 0.03	0.84 ± 0.04	0.33 ± 0.02
Nb1.8	48.61 ± 0.20	17.38 ± 0.09	9.11 ± 0.13	9.11 ± 0.20	7.28 ± 0.21	5.67 ± 0.07	1.64 ± 0.05	0.87 ± 0.04	0.34 ± 0.02

$$k'_i = \frac{C_i^{DC}}{C_i^{ID}} \quad \text{Eq. 4}$$

where C_i^{DC} and C_i^{ID} are an elements' concentration in the DC or ID region, respectively (concentration values listed in Table 5). The partitioning coefficient k'_i is plotted in Fig. 4a.

Fig. 4a shows the calculated partitioning coefficient k' as function of increasing Nb–Al ratio for the HESAs Nb1.2 (black diamond), Nb1.4 (blue squares), Nb1.6 (red triangles) and Nb1.8 (green circles). Ni, Co, Al, Fe, Cr and W with k'_i values > 1 partition towards DC regions and Ti, Nb and Mo with $k'_i < 1$ towards ID regions. Ti, Nb and W reveal the strongest partitioning tendency. Although the errors (standard deviations) are large, the increasing Nb–Al ratio appears to lessen the partitioning tendency of Fe, Nb, and Mo, and increases that of W. The partitioning behavior of Co and Cr is reversed (from ID to DC) with increasing Nb concentration. Ni and Co exhibit a k' value close to 1, indicating that these elements do not exhibit severe partitioning behavior. We note that the Nb1.8 alloy does not follow that trend.

In this study, significant challenges were encountered in the melting and homogenization of Nb, Mo, and W, attributed to the exceptionally high melting points of Nb (2741 K), Mo (2896 K), and W (3695 K). Furthermore, the propensity for the formation of NbTiMo-rich intermetallic phases, as reported by *Beneduce et al.* [52], was observed. Notably, an increase in the Nb–Al ratio appeared to exacerbate these difficulties. Insufficient melting time resulted in the incomplete fusion of Nb, leading to the formation of minimal, but distinct, insoluble intermetallic compounds. This observation underscores the complexity of processing these high-melting-point elements and their alloys, necessitating careful control of melting conditions to achieve desired material properties [53,54].

Fig. 4b compares two different methods for calculating the volume fraction of ID regions of our HESA alloys post-homogenization (1500 K/24 h). The lever rule is used to calculate the volume fraction of dendrite core (DC) and interdendritic (ID) regions based on EPMA data (represented by red squares), and this is compared to data obtained from image analysis of light microscopy images (blue circles). Both methods show a similar trend in changes. After a continuous decrease in the Nb1.2 and Nb1.4 alloys, the volume fraction of ID regions for Nb1.6 increases, followed by a decrease of 30–40 vol.% in Nb1.8.

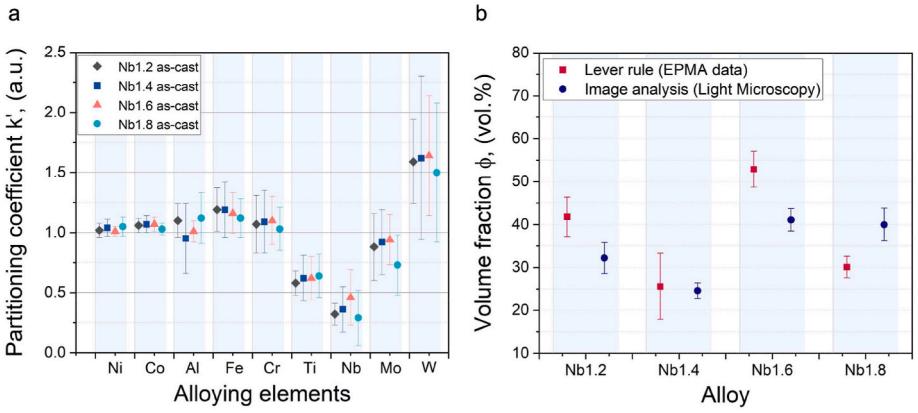

Fig. 4. Quantitative analysis of dendritic as-cast microstructure. (**a**) Partitioning coefficient k'_i for each alloying element i for Nb1.2 (black diamond), Nb1.4 (blue square), Nb1.6 (red triangle) and Nb1.8 (green circle) HESAs in as-cast condition. Calculated based on concentrations given in Table 5. (**b**) Volume fraction of ID regions of HESA as-cast alloys, from EPMA data (lever rule-based) and light-microscopy (image analysis). The errors are standard deviation σ and calculated based on counting statistics and standard error propagation methods [51].

3.3. Hierarchical microstructure

Fig. 5a–d illustrate SEM-SE images of our Nb1.2, Nb1.4, Nb1.6 and Nb1.8 alloys, respectively, with varying Nb–Al ratios after homogenization (1500 K/24 h) and aging 1023 K/10 h. None of the alloys exhibit secondary phases or any obvious macroscale heterogeneities. The images show only a negligible amount of pores and minor scratches resulting from the metallographic preparation.

Fig. 6a–d highlight high-magnification DF-TEM images of Nb1.2, Nb1.4, Nb1.6 and Nb1.8 alloys after 1500 K/24 h and 1023 K/10 h. We observe hierarchical microstructures, characterized by a γ matrix (A1, dark) with γ' precipitates ($L1_2$, bright) that contain further γ particles (A1, dark). A further enlarged view of the interior of γ' precipitates reveal a fine dispersion of γ particles (bottom row).

The inset shows the selected area electron diffraction (SAED) patterns of the [001] zone axis. Main reflections arise from {002}, {200} and {220} lattice planes within the disordered FCC γ matrix and the ordered γ' precipitates, however the weaker superlattice reflections {100}, {010}, {110} only originate from Ni-rich planes (face center positions) in $L1_2$-ordered γ' precipitates. We observe are nano–size particles inside the cuboidal γ' precipitate. The nano-size particles are likely γ phase, due to the absence of other spots in the SAED patterns.

γ' precipitates present an irregular mostly cubic morphology, indicative of a small lattice misfit [55–57]. The size of γ' precipitates appear to decrease with increasing Nb–Al ratio, when further aged at 1023 K/10 h. The morphology of γ particles remains spherical with increasing Nb–Al ratio. Similar observations, i.e., irregularly shaped γ' precipitates and spherical γ particles after aging, were also made in a high refractory-containing Ni-based superalloy [58].

3.3.1. Precipitate size

To compare the effect of varying the Nb–Al ratio on the microstructure, quantitative analysis of various phases within the alloys was conducted by introducing the equivalent radius $<R>$ and the volume fraction $<V>$, based on TEM images of each alloy (Fig. 7a and b). Microstructure analysis is achieved by applying a thresholding procedure in *ImageJ* [59]. All errors are standard deviation σ.

The average equivalent radius $<R>$ is defined as $R = (A/\pi)^{0.5}$, with A representing the area of a γ' precipitate or a γ particle. For each state (1500 K/24 h and 1023 K/10 h) five images, and a total of at least 100 γ' precipitates and 150 γ particles were considered. Fig. 7a shows their $<R>$ as function of increasing Nb–Al ratio. Our results indicate that overall, $<R_{\gamma'}>$ of γ' precipitates (blue squares) are decreasing with decreasing Nb–Al ratio (within the error). However, it appears that $<R_{\gamma'}>$ of the Nb1.6 alloy is larger compared to the Nb1.2 (base) alloy. This may possibly arise from the irregular shape of γ' precipitates and how they are contained in the TEM lamella (thickness of about 50 nm). A decreasing size of γ' precipitates was attributed to an addition of about 0.9 at.% Nb in a similar Ni-based superalloy (RRHT1 & RRHT3) [60]. We observe $<R_{\gamma}>$ of γ particles (red circles) to decrease as function of increasing Nb–Al ratio (appears constant within the error). We attribute the relatively larger error to inaccuracies when determining the size of γ particles from DF-TEM images during image analysis. The thickness of a TEM foil is ~50 nm and the γ particle size in the range of 3–4 nm, leading to strong contrast variations and overlap of γ particles. We note that the reported error reflects the standard deviation in size distribution among γ' precipitates and γ particles, highlighting the natural variability within the sample rather than experimental inaccuracies.

3.3.2. Comparison of volume fractions

In our study, the volume fractions of γ' precipitates and γ particles were evaluated using two distinct methodologies: TEM image analysis and lever rule approach utilizing equilibrium phase compositions based on ThermoCalc simulations (Table 7). Fig. 7b is a comparison of γ' precipitate volume fractions V_p obtained from TEM image analysis (blue squares) and ThermoCalc equilibrium phase compositions given in Table 7 (blue open squares), after homogenization (1500 K/24 h) and aging at 1023 K/10 h. In addition, the volume fraction of γ particles from TEM image analysis is also given (red circles). The results from these approaches, as shown in Fig. 7b, reveal significant differences as has been shown in the literature [33].

TEM image analysis: TEM image analysis typically involves the visual quantification of phase areas, which are then converted into volume fractions using geometric assumptions. In this study, TEM-derived volume fractions are obtained by analyzing dark-field images, employing a binarization and thresholding method to distinguish between γ and γ' phases. The analysis indicates a steady decrease in the volume fraction of γ' precipitates with increasing Nb–Al ratio. This trend is visually represented by a linear fit (blue line) across the data points (blue squares) presented in Fig. 7b. However, TEM techniques can potentially overestimate volume fractions due to several factors:

- **Contrast and brightness:** Variations in image contrast and brightness settings can alter the perception of phase boundaries and sizes.
- **Thresholding techniques:** The choice of thresholding can lead to either the inclusion or exclusion of borderline areas, affecting the estimated phase volumes.
- **Two-dimensional projection:** TEM images represent a two-dimensional projection of a three-dimensional structure, which may lead to inaccuracies when phases are unevenly distributed throughout the sample thickness.

ThermoCalc simulations and the lever rule method: ThermoCalc provides a theoretical estimation of equilibrium phase compositions. For the γ' precipitates, we used the lever rule approach, which generally results in lower estimated volume fractions (blue open squares) compared to TEM [33]. This difference of 20–30 vol.% indicates a systematic variation likely due to the fundamental nature of the methods:

- **Equilibrium assumptions:** ThermoCalc assumes a perfect equilibrium state, which may not be fully achievable in practical scenarios, particularly when kinetic factors play a significant role.

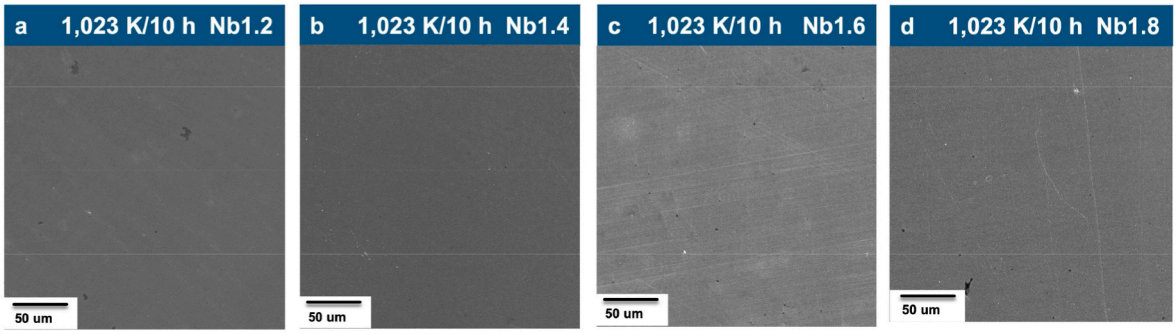

Fig. 5. SEM-SE images of HESAs Nb1.2, Nb1.4, Nb1.6, and Nb1.8 after homogenization (1500 K/24 h) and aging (1023 K/10 h).

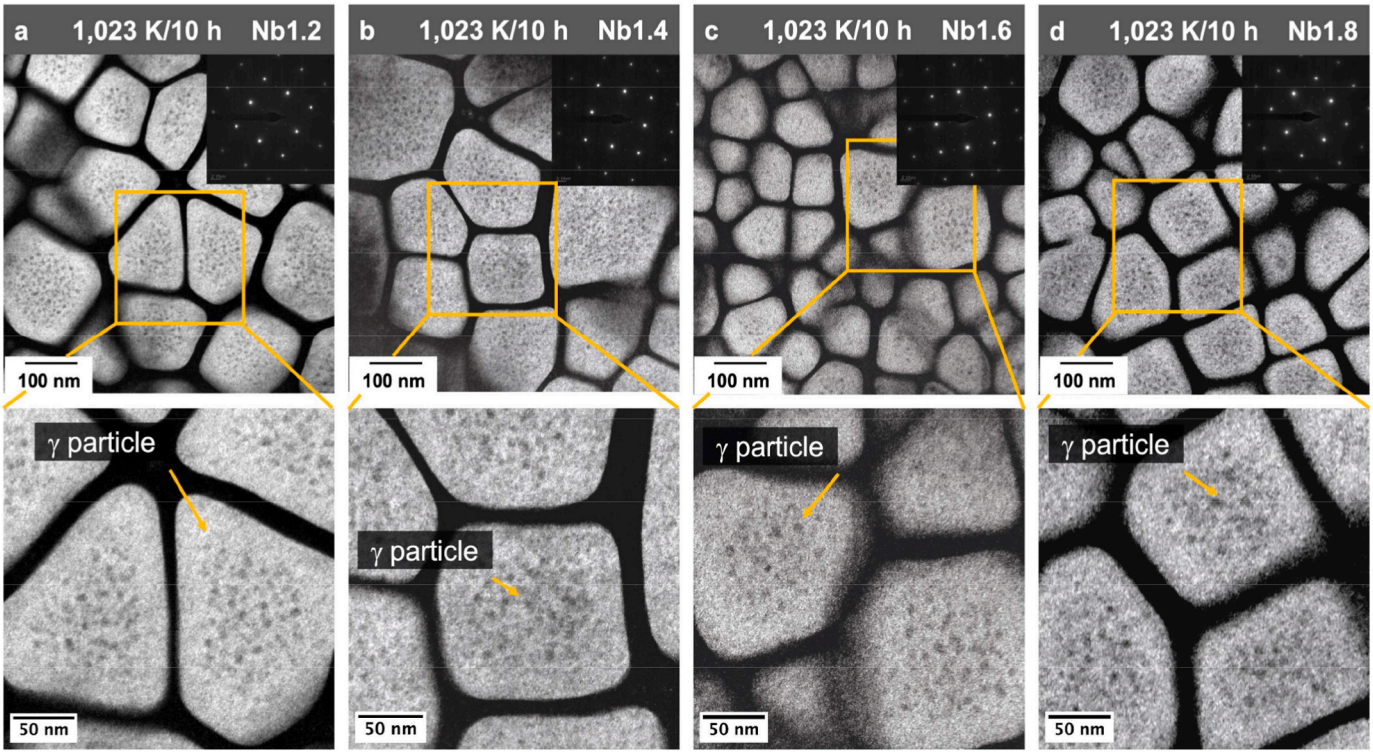

Fig. 6. DF-TEM images of HESAs Nb1.2, Nb1.4, Nb1.6, and Nb1.8 after homogenization (1500 K/24 h) and aging 1023 K/10 h. Images taken with an $L1_2$ superlattice reflection shown in the SAED in the inset. The γ matrix (dark) surrounds γ' precipitates (bright) that contain small spherical γ particles (dark).

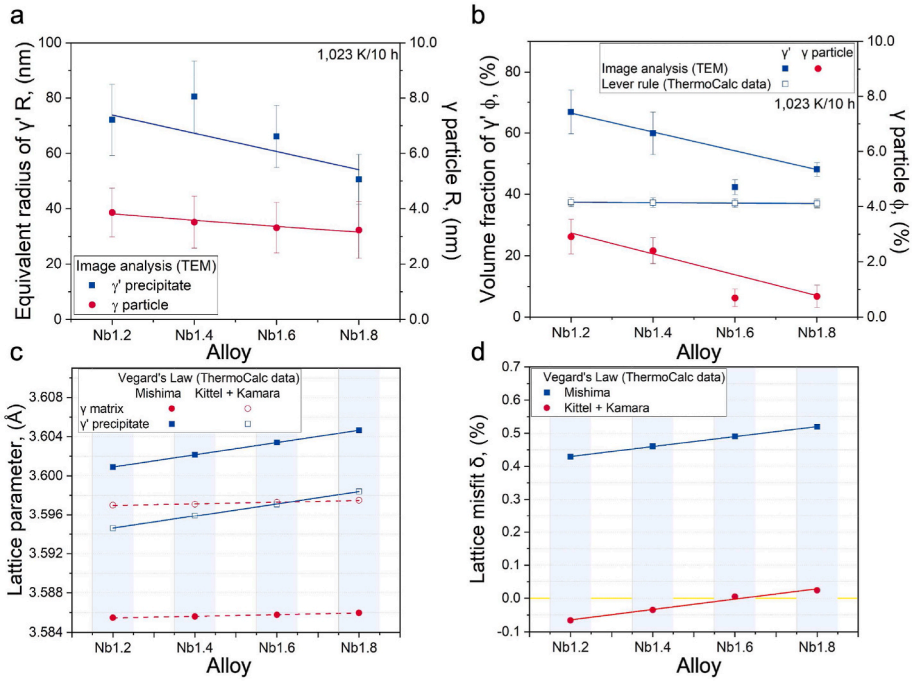

Fig. 7. (**a**) Equivalent radius of γ' precipitates (blue squares) and γ particles (red circles) based on TEM images of HESAs Nb1.2, Nb1.4, Nb1.6, and Nb1.8 after homogenization (1500 K/24 h) and aging 1023 K/10 h. (**b**) Volume fractions *f* of γ' precipitates from TEM image analysis (blue squares) and ThermoCalc compositions based lever rule (blue open squares), and γ particles (red circles) from TEM after homogenization (1500 K/24 h) and 1023 K/10 h. (**c**) Calculated lattice parameters of γ matrix (red circles) and γ' precipitates (blue squares) based on Vegard's law for parameters from group 1 (solid symbols) and group 2 (open symbols) and ThermoCalc equilibrium phase compositions at 1023 K. (**d**) Calculated lattice misfit from lattice parameters shown in (**c**) for group 1 parameters (blue squares) and group 2 (red circles). The errors are standard deviation σ and calculated based on counting statistics and standard error propagation methods [51].

Table 7
Equilibrium compositions (in at.%) of γ and γ' phases at 1023 K simulated for each alloy using ThermoCalc [31] and the TTNi12 database [32].

Alloy	Phase	Concentration, (at.%)								
		Ni	Co	Al	Fe	Cr	Ti	Nb	Mo	W
Nb1.2	γ	28.04	27.51	2.42	23.33	17.42	0.30	0.14	0.14	0.71
	γ'	61.88	11.17	13.83	2.06	0.60	8.74	1.65	0.02	0.05
Nb1.4	γ	27.64	27.78	2.38	23.52	17.42	0.30	0.16	0.13	0.66
	γ'	62.00	11.07	13.63	2.01	0.58	8.72	1.92	0.02	0.05
Nb1.6	γ	27.21	28.06	2.33	23.72	17.44	0.30	0.19	0.13	0.61
	γ'	62.11	10.98	13.43	1.97	0.55	8.70	2.20	0.02	0.04
Nb1.8	γ	26.82	28.34	2.29	23.90	17.44	0.31	0.21	0.13	0.57
	γ'	62.22	10.89	13.23	1.93	0.52	8.68	2.48	0.01	0.04

- **Compositional accuracy:** The accuracy of ThermoCalc predictions depends heavily on the correctness and completeness of the compositional data and phase diagrams used in the calculations.

To bridge the gap between empirical observations and theoretical predictions, more work is needed, ideally incorporating APT data to obtain direct measurements of phase chemistry. APT offers high-resolution compositional analysis at the atomic level, which can be crucial for accurately calculating phase volume fractions using direct methods rather than relying on image-based estimations.

By aligning TEM observations with ThermoCalc and future APT data, we can refine our understanding of material behaviors and optimize alloy compositions more effectively. This integrated approach will enable a more accurate prediction and manipulation of microstructural features to achieve desired material properties.

3.3.3. Lattice parameter and misfit

We derive the lattice parameters of γ matrix and γ' precipitate phases as function of Nb–Al ratio using Vegard's law and ThermoCalc equilibrium phase compositions at 1023 K (given in Table 7) as:

$$\alpha_{\gamma} = \alpha_{0(\mathrm{Ni})} + \sum V_i^{\gamma} C_i^{\gamma}$$

$$\alpha_{\gamma'} = \alpha_{0(\mathrm{Ni3Al})} + \sum V_i^{\gamma'} C_i^{\gamma'} \qquad \text{Eq. 5}$$

where α_{Ni} and α_{Ni3Al} are the lattice parameters of pure Ni and pure Ni_3Al, V_i^{γ} and $V_i^{\gamma'}$ are the Vegard's coefficients for the element i in Ni and Ni_3Al respectively, and C_i^{γ} and $C_i^{\gamma'}$ are the concentration of element i in γ matrix and γ' precipitate phase.

We calculate the lattice parameters based on values for Ni and Ni_3Al from three different references, *Mishima et al.* [61], *Kittel* [62] and *Kamara et al.* [63]. In this manner, we build two groups: (1) Ni and Ni_3Al from *Mishima et al.* and (2) Ni from *Kittel* and Ni_3Al from *Kamara et al.* [63], given in Table 8.

All Vegard's coefficients for Ni, Co, Al, Fe, Cr Ti, Nb, Mo, W in the γ matrix and the γ' precipitate phase is taken from *Mishima et al.* [61].

Fig. 7c illustrates the evolution of lattice parameters as function of Nb–Al ratio for group 1 (solid symbols) and group 2 (open symbols), where the γ matrix is represented by red circles and γ' precipitates by blue squares. The lines are linear fits. In both groups, the lattice parameter of the γ matrix increases only slightly (within 0.0005 Å), whereas that of γ' precipitates increase markedly (within 0.004 Å). We note, that a_{γ} of group 1 is about 0.01 Å lower compared with group 2, and $a_{\gamma'}$ of group 1 is about 0.006 Å larger compared with group 2.

From calculated lattice parameters (Fig. 7c), we obtain the lattice misfit δ between the γ matrix and γ' precipitates as:

$$\delta = \frac{2(\alpha_{\gamma'} - \alpha_{\gamma})}{(\alpha_{\gamma'} + \alpha_{\gamma})} \qquad \text{Eq. 6}$$

Fig. 7d presents the lattice misfit δ as function of increasing Nb–Al ratio derived from lattice parameters of group 1 (blue square) and group 2 (red circles). The lines are linear fits. We generally observe an increasing lattice misfit with increasing Nb–Al ratio. For group 1 (*Mishima et al.*) [61] lattice parameters, the lattice misfit is positive (0.43–0.52 %). For group 2 (*Kittel* + *Kamara et al.*) [62,63] lattice parameters, the lattice misfit is initially negative (−0.06 % for Nb1.2) and eventually becomes positive (0.02 % for Nb1.8).

The lattice constant is intricately linked to the distribution of alloying elements within the γ' and γ phases. The precise arrangement of these elements significantly influences the structural characteristics and lattice parameters of both phases. The relative size of Nb atoms in comparison to the base metal can induce either lattice expansion or contraction, thereby exerting a profound impact on the overall structural behavior of the alloy. The addition of Nb, with its larger atomic radius, influences lattice expansion and segregation behavior, impacting the lattice parameters and, consequently, the overall microstructure and mechanical properties of the alloy [64]. In alloys having a larger misfit, elongation, and directional alignment of γ particles are typically observed [14,58,65,66]. This behavior is a function of elastic constants, interfacial energy, and particle size [58].

Table 8
Literature data for lattice parameters of γ matrix (Ni) and γ' precipitate (Ni_3Al) phases.

Reference	a_0(Ni), (Å)	a_0(Ni_3Al), (Å)
Mishima et al. 1985 [61]	3.524	3.570
Kittel 2005 [62]	3.5355	–
Kamara 1996 [63]	–	3.5637

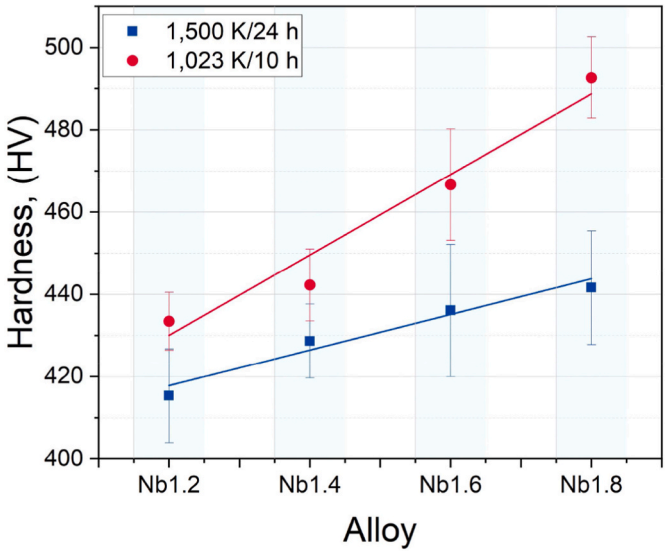

Fig. 8. Vickers hardness of HESAs Nb1.2, Nb1.4, Nb1.6 and Nb1.8 after homogenization at 1500 K/24 h (blue squares) and subsequent aging at 1023 K/10 h (red circles). The errors are standard deviation σ and calculated based on counting statistics and standard error propagation methods [51].

Fig. 8a presents the room temperature Vickers hardness as function of increasing Nb–Al ratio of samples after 1500 K/24 h (blue square) and after aging at 1023 K/10 h (red circles). The lines are linear fits. We generally observe an increasing hardness with increasing Nb–Al ratio for both conditions (homogenized 1500 K/24 h and aged at 1023 K/10 h). Furthermore, we observe a higher hardness of the 1023 K/10 h aged samples, increasing at a steeper rate with increasing Nb–Al ratio, compared to the homogenized samples (from +15 HV to +50 HV).

This investigation reveals a distinct inhibitory effect of the Nb–Al ratio on the formation of γ particles. This inhibition is evident through the reduction in both the radius and volume fraction of γ particles with increasing Nb–Al ratio. Furthermore, the increasing Nb–Al ratio correlates with a diminished size of γ' precipitates, we attribute this to the sluggish diffusivity of Nb, which exerts a more pronounced impact on microstructure kinetics at higher concentrations. The slow diffusivity of Nb is the rate controlling factor for the mobility of γ-forming species in the Ni_3Al γ' precipitate phase, thereby defining the kinetics of formation and evolution of γ particles. Our findings highlight the role of Nb in significantly augmenting the lattice parameter of γ' precipitates relative to that of the γ matrix, resulting in a diminishing lattice misfit, gradually approaching zero from the negative. The effectiveness of our 1023 K/10 h aging treatment is shown by Vickers hardness measurements, showcasing superior mechanical performance in the 1023 K/10 h aged samples. Consequently, we conclude that the enhancement in mechanical properties is predominantly attributable to the influence of Nb on the overall microstructure and γ' precipitates.

Our research demonstrates a significant advancement in the manipulation of key microstructural parameters in Ni-based superalloys and high-entropy superalloys through the strategic incorporation and manipulation of Nb. The experimental findings clearly illustrate that Nb plays a crucial role in controlling the size, volume fraction, and lattice parameters/misfit of the γ particles. Notably, as the Nb–Al ratio increases, there is a marked decrease in both the size and volume fraction of γ particles, suggesting that Nb effectively either inhibits the formation kinetics of γ particles or reduces their overall equilibrium volume fraction. This is in line with the established role of Nb as a γ'-former, confirming its anticipated behavior in these complex alloys. Further studying those samples aged at 1023 K/10 h after aging for longer times is necessary to clarify whether or not Nb has slowed down the kinetic evolution or merely reduced the volume fraction of γ particles.

Our study further provides a clear "proof of concept" that manipulating the Nb–Al ratio allows for precise control over these three critical parameters. Computational work based on phase-field modeling suggested that manipulation of hierarchical γ particles may be possible through parameters such as interfacial energy, solute diffusivity and supersaturation of γ-former solutes (within γ' precipitates) to enhance their stability [58]. By tuning the Nb–Al ratio, we can deliberately influence the microstructural characteristics of the alloy and the hierarchical γ particles. This finding is crucial as it opens up new avenues for tailoring the properties of Ni-based and high-entropy superalloys to meet specific performance requirements through improved microstructural stability. The ability to control the size, volume fraction, and lattice misfit of hierarchical γ particles through the Nb–Al ratio adjustment not only enhances our understanding of the alloys' behavior but also paves the way for the development of materials with optimized mechanical properties for high-temperature applications.

This insight into the role of Nb provides a valuable framework for future alloy design of high-temperature structural materials strengthened by hierarchical microstructures, emphasizing the importance of alloying elements in achieving desired material characteristics.

4. Conclusions

The variation of Nb (balanced by Al), i.e., the Nb–Al ratio, as a γ'-forming element in HESAs induces modifications in the as-cast dendritic microstructure, consequently influencing the homogenization behavior. For our experimental alloys (Nb = 1.2–1.8 at.%), the following conclusions on the homogenization behavior can be made:

1. **Microstructure of as-Cast HESAs:** The four HESA alloys exhibit distinct dendritic as-cast microstructures with dendrite core (DC) and interdendritic (ID) regions, with primary dendrite arm spacing (PDAS) averaging between 66 and 73 μm.
2. **Homogenization parameters**: A homogenization temperature range of 1450–1510 K was established, with a timeframe of 4 h at 1500 K identified as sufficient for effective homogenization (DSC and diffusion calculations). These homogenization conditions were verified as effective by EPMA analysis.
3. **Elemental segregation and homogenization:** EPMA analysis indicated elemental segregation in as-cast alloys, becoming uniform after homogenization. Elements like Ni, Co, Al, Fe, Cr, and W ($k'_i > 1$) prefer dendritic cores, whereas Ti, Nb, and Mo ($k'_i < 1$) favor interdendritic regions. Increased Nb shifts Co and Cr from interdendritic to dendritic regions, with Ni and Co showing minimal segregation.
4. **γ' Precipitate stability**: The decreasing γ' precipitate solvus temperature with increased Nb–Al ratio suggests Nb's significant role in influencing the stability of these precipitates in HESAs.
5. **Influence of arc-melting:** Arc-melting, characterized by rapid cooling, resulted in smaller PDAS values in HESAs compared to singly crystal casting, underscoring the impact of manufacturing processes on alloy microstructures.

The impact of the Nb-Al ratio on the development of hierarchical microstructures, the morphology of γ particles, volume fraction, and lattice parameters allows the following conclusions:

1. **Microstructure and precipitate morphology:** DF-TEM images depict hierarchical microstructures in all four HESAs comprising a γ matrix, γ' precipitates, and γ particles. Indicating that the range between 1.2 and 1.8 at.% Nb enables the formation of hierarchical microstructures.
2. **Quantitative analysis of microstructure:** $<R>$ analysis reveals a decrease in $<R_{\gamma'}>$ of γ' precipitates and $<R_{\gamma}>$ of γ particles with increasing Nb–Al ratio. Volume fraction analysis demonstrates a consistent decrease in TEM-derived γ' precipitate volume fractions, supported by predictions made by ThermoCalc.
3. **Lattice parameters and misfit**: Using Vegard's law with ThermoCalc data at 1023 K, lattice parameters for the γ matrix show a slight increase, while γ' precipitates see a more pronounced rise with increasing Nb–Al ratio. Consequently, the lattice misfit (δ) also increases, highlighting Nb's significant impact on lattice parameters and misfit.
4. Manipulation of size, volume fraction and lattice parameter of γ particles is achievable by intricately tuning the alloys' composition.
5. Nb as a γ'-forming element affects γ particles in the anticipated way: The increasing content is increasingly inhibiting the formation of γ particles within γ' precipitates.

CRediT authorship contribution statement

Yiqin Ma: Writing – original draft, Visualization, Software, Investigation, Formal analysis. **Qiuying Ji:** Visualization, Investigation, Formal analysis. **Sieglind Ngai:** Writing – review & editing, Supervision, Resources, Conceptualization. **Jingzhen Li:** Visualization, Investigation, Formal analysis. **Michael J. Pavel:** Writing – review & editing, Visualization, Software, Formal analysis. **Mark L. Weaver:** Writing – review & editing, Software, Resources. **Peng Zhang:** Writing – review & editing, Visualization, Investigation. **Wei Li:** Writing – review & editing, Supervision, Methodology, Investigation. **Yuan Wu:** Writing – review & editing, Resources, Formal analysis. **Florian Vogel:** Writing – review & editing, Supervision, Methodology, Investigation, Conceptualization.

Declaration of competing interest

The authors declare that they have no known competing financial interests or personal relationships that could have appeared to influence the work reported in this paper.

Data availability

No data was used for the research described in the article.

Acknowledgements

F.V. acknowledges financial support by the National Natural Science Foundation of China (NSFC grant No. 52150610488), the National Natural Science Foundation of Guangdong, China (grant No. 2021A1515010563), the State Key Lab of Advanced Metals and Materials (grant No. 2021-ZD09). M.J.P. and M.L.W. were partially supported by the National Science Foundation (DMR-2105364). This work was supported by Nova Scientific (Guangzhou) Co., Ltd. (www.novascitech.com) specifically Lin Chen and Valerie Du are gratefully acknowledged for their help with SEM, FIB-TEM sample preparation and TEM imaging. The authors acknowledge the use of ChatGPT 4.0 [https://chat.openai.com/] for enhancing the language and readability of this document.

References

[1] B. Cantor, I. Chang, P. Knight, A. Vincent, Microstructural development in equiatomic multicomponent alloys, Mater. Sci. Eng., A 375–377 (2004) 213–218.
[2] Y.T. Chen, Y.J. Chang, H. Murakami, T. Sasaki, K. Hono, C.W. Li, et al., Hierarchical microstructure strengthening in a single crystal high entropy superalloy, Sci. Rep. 10 (2020), https://doi.org/10.1038/s41598-020-69257-8.
[3] E.P. George, W.A. Curtin, C.C. Tasan, High entropy alloys: a focused review of mechanical properties and deformation mechanisms, Acta Mater. 188 (2020) 435–474, https://doi.org/10.1016/j.actamat.2019.12.015.
[4] J.W. Yeh, S.K. Chen, S.J. Lin, J.Y. Gan, T.S. Chin, T.T. Shun, et al., Nanostructured high-entropy alloys with multiple principal elements: novel alloy design concepts and outcomes, Adv. Eng. Mater. 6 (2004) 299–303, https://doi.org/10.1002/adem.200300567.
[5] T.K. Tsao, A.C. Yeh, C.M. Kuo, K. Kakehi, H. Murakami, J.W. Yeh, et al., The high temperature tensile and creep behaviors of high entropy superalloy, Sci. Rep. 7 (2017), https://doi.org/10.1038/s41598-017-13026-7.
[6] J.W. Yeh, S.K. Chen, S.J. Lin, J.Y. Gan, S.Y. Chang, Microstructural control and properties optimization of high-entropy alloys, Adv. Eng. Mater. 6 (2004) 299–303.
[7] T. Saito, Y.T. Chen, Y. Takata, K. Kawagishi, W.C. Hsu, A.C. Yeh, et al., Effect of heat treatments on the microstructural evolution of a single crystal high-entropy superalloy, Metals 10 (2020) 1–17, https://doi.org/10.3390/met10121600.
[8] F. Otto, A. Dlouhý, C. Somsen, H. Bei, G. Eggeler, E.P. George, The influences of temperature and microstructure on the tensile properties of a CoCrFeMnNi high-entropy alloy, Acta Mater. 61 (2013) 5743–5755, https://doi.org/10.1016/j.actamat.2013.06.018.
[9] Z. Wu, H. Bei, F. Otto, G.M. Pharr, E.P. George, Recovery, recrystallization, grain growth and phase stability of a family of FCC-structured multi-component equiatomic solid solution alloys, Intermetallics 46 (2014) 131–140, https://doi.org/10.1016/j.intermet.2013.10.024.
[10] A.V. Kuznetsov, D.G. Shaysultanov, N.D. Stepanov, G.A. Salishchev, O.N. Senkov, Tensile properties of an AlCrCuNiFeCo high-entropy alloy in as-cast and wrought conditions, Mater. Sci. Eng., A 533 (2012) 107–118, https://doi.org/10.1016/j.msea.2011.11.045.
[11] G.P.M. Leyson, W.A. Curtin, Solute strengthening at high temperatures, Model. Simulat. Mater. Sci. Eng. 24 (2016), https://doi.org/10.1088/0965-0393/24/6/065005.
[12] E.P. George, W.A. Curtin, C.C. Tasan, High entropy alloys: a focused review of mechanical properties and deformation mechanisms, Acta Mater. 188 (2020) 435–474, https://doi.org/10.1016/j.actamat.2019.12.015.
[13] M. Joele, W.R. Matizamhuka, A review on the high temperature strengthening mechanisms of high entropy superalloys (Hesa), Materials 14 (2021), https://doi.org/10.3390/ma14195835.
[14] F. Vogel, N. Wanderka, Z. Balogh, M. Ibrahim, P. Stender, G. Schmitz, et al., Mapping the evolution of hierarchical microstructures in a Ni-based superalloy, Nat. Commun. 4 (2013) 1–7, https://doi.org/10.1038/ncomms3955.
[15] G. Song, Z. Sun, J.D. Poplawsky, Y. Gao, P.K. Liaw, Microstructural evolution of single Ni2TiAl or hierarchical NiAl/Ni2TiAl precipitates in Fe-Ni-Al-Cr-Ti ferritic alloys during thermal treatment for elevated-temperature applications, Acta Mater. 127 (2017) 1–16, https://doi.org/10.1016/j.actamat.2017.01.011.
[16] F. Vogel, N. Wanderka, Z. Balogh, M. Ibrahim, P. Stender, G. Schmitz, et al., Mapping the evolution of hierarchical microstructures in a Ni-based superalloy, Nat. Commun. 4 (2013), https://doi.org/10.1038/ncomms3955.
[17] E. Zaiser, X.Y. Zhou, A.M. Manzoni, S. Haas, U. Glatzel, X.P. Zhang, et al., Hierarchical phase separation behavior in a Ni-Si-Fe alloy, Acta Mater. 195 (2020) 327–340.
[18] S. Hata, K. Kimura, H. Gao, S. Matsumura, M. Doi, T. Moritani, et al., Electron tomography imaging and analysis of γ′ and γ domains in Ni-based superalloys, Adv. Mater. 20 (2008) 1905–1909, https://doi.org/10.1002/adma.200702461.
[19] F. Vogel, S. Ngai, X.Y. Zhou, E. Zaiser, A.M. Manzoni, Y. Wu, et al., Tracking maze-like hierarchical phase separation behavior in a Fe-Si-V alloy, J. Alloys Compd. 968 (2023), https://doi.org/10.1016/j.jallcom.2023.172157.
[20] M. Huang, Y. Ma, Y. Wu, W. Zheng, M.J. Pavel, M.L. Weaver, et al., Effect of γ forming element additions on the homogenization behavior and formation of hierarchical microstructures in Ni-based superalloys, J. Alloys Compd. 975 (2024), https://doi.org/10.1016/j.jallcom.2023.172929.
[21] G. Song, Z. Sun, L. Li, X. Xu, M. Rawlings, C.H. Liebscher, et al., Ferritic alloys with extreme creep resistance via coherent hierarchical precipitates, Sci. Rep. 5 (2015), https://doi.org/10.1038/srep16327.
[22] M.S. Titus, Y.M. Eggeler, A. Suzuki, T.M. Pollock, Creep-induced planar defects in L12-containing Co- and CoNi-base single-crystal superalloys, Acta Mater. 82 (2015) 530–539, https://doi.org/10.1016/j.actamat.2014.08.033.
[23] S. Meher, L.K. Aagesen, M.C. Carroll, T.M. Pollock, L.J. Carroll, The origin and stability of nanostructural hierarchy in crystalline solids, Sci. Adv. 4 (2018) eaao6051.
[24] Y. Kuno, Y. Nakane, T. Kozakai, M. Doi, J. Yamanaka, C. Yamamoto, et al., Phase-separation of B2 precipitates in an Fe-Ni-Al alloy, Mater. Sci. Forum 638–642 (2010) 2274–2278. https://doi.org/10.4028/www.scientific.net/MSF.638-642.2274.
[25] M. Doi, T. Moritani, T. Kozakai, M. Wakano, Transmission electron microscopy observations of the phase separation of $D0_3$ precipitates in an elastically constrained Fe-Si-V alloy, ISIJ Int. 46 (2006) 155–160, https://doi.org/10.2355/isijinternational.46.155.
[26] S. Antonov, D. Isheim, D.N. Seidman, E. Sun, R.C. Helmink, S. Tin, γ′ phase instabilities in high refractory content γ-γ′ Ni-base superalloys, in: M. Hardy, E. Huron, U. Glatzel, B. Griffin, B. Lewis, C. Rae, et al. (Eds.), Superalloys 2016: 13th International Symposium on Superalloys, the Minerals, Metals & Materials Society, 2016, pp. 199–208, https://doi.org/10.1002/9781119075646.ch22.
[27] M.K. Miller, S.S. Babu, J.M. Vitek, Stability of γ′ precipitates in a PWA1480 alloy, Intermetallics 15 (2007) 757–766, https://doi.org/10.1016/j.intermet.2006.10.030.
[28] M. Senga, H. Kumagai, T. Moritani, M. Doi, Transmission electron microscopy (TEM) observations of phase-separations of gamma-prime precipitates in Ni-Al-Fe and Ni-Si-Fe ternary alloys, Adv. Mater. Res. 26–28 (2007) 1311–1314. https://doi.org/10.4028/www.scientific.net/AMR.26-28.1311.
[29] T. Moritani, M. Ota, T. Kozakai, M. Doi, TEM observations of two-phase microstructure formed by phase separation of gamma-prime precipitates in Ni-Al-Si alloys, Mater. Sci. Forum 561–565 (2007) 2361–2364. https://doi.org/10.4028/www.scientific.net/MSF.561-565.2361.
[30] M. Huang, Y. Ma, Y. Wu, W. Zheng, M.J. Pavel, M.L. Weaver, et al., Effect of γ forming element additions on the homogenization behavior and formation of hierarchical microstructures in Ni-based superalloys, J. Alloys Compd. 975 (2024) 172929, https://doi.org/10.1016/j.jallcom.2023.172929.
[31] J.O. Andersson, T. Helander, L. Höglund, P. Shi, B. Sundman, Thermo-Calc & DICTRA, computational tools for materials science, Calphad 26 (2002) 273–312, https://doi.org/10.1016/S0364-5916(02)00037-8.
[32] TCS High Entropy Alloys Database (TCHEA6). (n.d).
[33] F. Vogel, S. Ngai, X.Y. Zhou, E. Zaiser, A.M. Manzoni, Y. Wu, et al., Tracking maze-like hierarchical phase separation behavior in a Fe-Si-V alloy, J. Alloys Compd. 968 (2023), https://doi.org/10.1016/j.jallcom.2023.172157.
[34] H.J. Maier, T. Niendorf, R. Bürgel, Handbuch Hochtemperatur-Werkstofftechnik, Springer-Verlag, 2011.
[35] K.O. Yu, Solidification Modeling of Single-Crystal Investment Castings n.D, 1990.
[36] R.M. Kearsey, J.C. Beddoes, P. Jones, P. Au, Compositional design considerations for microsegregation in single crystal superalloy systems, Intermetallics 12 (2004) 903–910, https://doi.org/10.1016/j.intermet.2004.02.041.
[37] P. Hallensleben, H. Schaar, P. Thome, N. Jöns, A. Jafarizadeh, I. Steinbach, et al., On the evolution of cast microstructures during processing of single crystal Ni-base superalloys using a Bridgman seed technique, Mater. Des. 128 (2017) 98–111, https://doi.org/10.1016/j.matdes.2017.05.001.
[38] C. Rodenkirchen, A.K. Ackerman, P.M. Mignanelli, A. Cliff, G.J. Wise, P. Breul, et al., Effect of alloying on the microstructure, phase stability, hardness, and partitioning behavior of a new dual-superlattice nickel-based superalloy, Metall Mater Trans A Phys Metall Mater Sci 54 (2023) 1902–1923, https://doi.org/10.1007/s11661-023-06972-7.
[39] K.A. Christofidou, M.C. Hardy, H.Y. Li, C. Argyrakis, H. Kitaguchi, N.G. Jones, et al., On the effect of Nb on the microstructure and properties of next generation polycrystalline powder metallurgy Ni-based superalloys, Metall Mater Trans A Phys Metall Mater Sci 49 (2018) 3896–3907, https://doi.org/10.1007/s11661-018-4682-4.
[40] S.R. Hegde, R.M. Kearsey, J.C. Beddoes, Designing homogenization-solution heat treatments for single crystal superalloys, Mater. Sci. Eng., A 527 (2010) 5528–5538, https://doi.org/10.1016/j.msea.2010.05.019.
[41] Karunaratne M, Cox D, Carter P, Reed R. MODELLING OF THE MICROSEGREGATION IN CMSX-4 SUPERALLOY AND ITS HOMOGENISATION DURING HEAT TREATMENT. n.d.
[42] C.P. Heijwegen, G.D. Rieck, Determination of the phase diagram of the molybdenum-nickel system using diffusion couples and equilibrated alloys, Int. J. Mater. Res. 64 (1973) 450–453.

[43] M.J. Sohrabi, H. Mirzadeh, Estimation of homogenisation time for superalloys based on a new diffusional model, Mater. Sci. Technol. 36 (2020) 380–384, https://doi.org/10.1080/02670836.2019.1706906.
[44] P.D. Jablonski, J.A. Hawk, Homogenizing advanced alloys: thermodynamic and kinetic simulations followed by experimental results, J. Mater. Eng. Perform. 26 (2017) 4–13, https://doi.org/10.1007/s11665-016-2451-3.
[45] Janssen MMP. Diffusion in the Nickel-Rich Part of the Ni-AI System at 1000 ~ to 1300~ Ni3AI Layer Growth, Diffusion Coefficients, and Interface Concentrations. n.d.
[46] Q. Wu, S.S. Li, Y. Ma, S.K. Gong, First principles calculations of alloying element diffusion coefficients in Ni using the five-frequency model, Chin. Phys. B 21 (2012), https://doi.org/10.1088/1674-1056/21/10/109102.
[47] M.S. A Karunaratne, P. Carter, R.C. Reed, ON THE DIFFUSION OF ALUMINIUM AND TITANIUM IN THE Ni-RICH Ni-Al-Ti SYSTEM BETWEEN 900 AND 1200°C, 49, 2001.
[48] Dean DC, Goldstein JI. Determination of the Interdiffusion Coefficients in the Fe-Ni and Fe-Ni-P Systems below 900 ~. n.d.
[49] D.D. Pruthi, M.S. Anand, R.P. Agarwala, Diffusion of chromium in inconel-600, J. Nucl. Mater. 64 (1977) 206–210, https://doi.org/10.1016/0022-3115(77)90026-5.
[50] Walsh JM, Donachie MJ, Met SME, Sc ADIM. Interdiffusion in the Nickel-Tungsten and Thoria-Dispersed Nickel-Tungsten Systems Are in the. n.d.
[51] L.G. Parratt, Probability and Experimental Errors in Science, John Wiley, New York, 1966.
[52] Beneduce F, Mitchell A, Cockcroft SL, Schmalz AJ. PRIMARY CARBIDE SOLUTION DURING THE MELTING OF SUPERALLOYS. n.d.
[53] C.J. Farnin, S. Orzolek, J.N. DuPont, A novel approach to determine variable solute partition coefficients, Metall Mater Trans A Phys Metall Mater Sci 51 (2020) 5771–5780, https://doi.org/10.1007/s11661-020-05986-9.
[54] Z. Liang, J.D.H. Paul, A. Stark, A. Bezold, S. Neumeier, M. Göken, et al., High-temperature CoNi-based superalloys strengthened by γ′-(Ni,Co)3(Cr,Al,Ti,X): the effect of refractory elements, Metall Mater Trans A Phys Metall Mater Sci 54 (2023) 1620–1634, https://doi.org/10.1007/s11661-022-06795-y.
[55] Y. Zhang, J. Li, H. Yu, J. Sun, Z. Wang, Q. Wang, Effect of Ti/Nb/Ta addition on high-temperature microstructural stability of coherent γ/γ′ in Ni–Al–(Cr,Mo,W) superalloys, J. Mater. Res. 38 (2023) 729–740, https://doi.org/10.1557/s43578-022-00857-y.
[56] A. Bezold, H.J. Stone, C.M.F. Rae, S. Neumeier, In situ investigation of TCP phase formation, stress relaxation and γ/γ′ lattice misfit evolution in fourth generation single crystal Ni-base superalloys by X-ray high temperature diffraction, Metall Mater Trans A Phys Metall Mater Sci 53 (2022) 2890–2901, https://doi.org/10.1007/s11661-022-06713-2.
[57] S. Huang, K. An, Y. Gao, A. Suzuki, Determination of γ/γ′ lattice misfit in Ni-based single-crystal superalloys at high temperatures by neutron diffraction, Metall Mater Trans A Phys Metall Mater Sci 49 (2018) 740–751, https://doi.org/10.1007/s11661-017-4455-5.
[58] S. Meher, L.K. Aagesen, M.C. Carroll, T.M. Pollock, L.J. Carroll, The origin and stability of nanostructural hierarchy in crystalline solids, Sci. Adv. 4 (2018) 1–10, https://doi.org/10.1126/sciadv.aao6051.
[59] ImageJ. https://imagej.nih.gov/ij/, 2018 (n.d.).
[60] S. Antonov, M. Detrois, D. Isheim, D. Seidman, R.C. Helmink, R.L. Goetz, et al., Comparison of thermodynamic database models and APT data for strength modeling in high Nb content γ-γ' Ni-base superalloys, Mater. Des. 86 (2015) 649–655, https://doi.org/10.1016/j.matdes.2015.07.171.
[61] Mishima' Y, Ochiai'f S, Suzuki' T. LATTICE PARAMETERS OF Ni(y), Ni3Al(y') AND Ni,Ga(y') SOLID SOLUTIONS WITH ADDITIONS OF TRANSITION AND B-SUBGROUP Elements. n.d.
[62] Introduction to Solid State Physics Charles Kittel, 2005.
[63] Kamara AB, Ardell AJ, Wagner CNJ. Lattice Misfits in Four Binary Ni-Base 7/3" Alloys at Ambient and Elevated Temperatures. n.d.
[64] K.A. Christofidou, M.C. Hardy, H.Y. Li, C. Argyrakis, H. Kitaguchi, N.G. Jones, et al., On the effect of Nb on the microstructure and properties of next generation polycrystalline powder metallurgy Ni-based superalloys, Metall Mater Trans A Phys Metall Mater Sci 49 (2018) 3896–3907, https://doi.org/10.1007/s11661-018-4682-4.
[65] F. Vogel, S. Ngai, K. Fricke, M. McKechnie, N. Wanderka, T. Hentrich, et al., Tracing the three-dimensional nanochemistry of phase separation in an inverse Ni-based superalloy, Acta Mater. 157 (2018) 326–338, https://doi.org/10.1016/j.actamat.2018.07.038.
[66] M. Doi, T. Miyazaki, The effect of elastic interaction energy on the shape of γ′-precipitate in Ni-based alloys, in: M. Gell, C.S. Kortovich, R.H. Bricknell, W. B. Kent, J.F. Radavich (Eds.), Superalloys 1984, Warrendale, Pensylvania, USA: the Minerals, Metals & Materials Society, 1984, pp. 543–552.